Dalton Transactions

Accepted Manuscript

ROYAL SOCIETY OF CHEMISTRY

www.rsc.org/dalton

Non-covalent functionalization of WS_2 monolayer with small fullerenes: Tuning electronic properties and photoactivity

Cai-Yun Luo[1], Wei-Qing Huang[1*], Wangyu Hu[2], P. Peng[2], Gui-Fang Huang[1#]

[1] Department of Applied Physics, School of Physics and Electronics, Hunan University, Changsha 410082, China

[2] School of Materials Science and Engineering, Hunan University, Changsha 410082, China

Abstract: Atomically thin two-dimensional transition metal dichalcogenides (TMDCs) heterostructures have recently attracted growing interest due to their massive potentials for solar energy applications due to their band gap in the visible spectral range and extremely strong light–matter interactions. Herein, the heterostructures composed of WS_2 and MoS_2 monolayers, as representatives of TMDCs, with small fullerene (B_{12} and C_{20}) are investigated to explore their applications in solar energy conversion by using first-principles calculations based on density functional theory (DFT). WS_2 (MoS_2) monolayer and fullerene form a van der Waals (vdW) heterostructures. Compared to pure monolayers, the heterostructures have smaller band gap, which is in favor of enhancing the visible light absorption. The amount of charge transfer at interface induced by vdW interaction depends on the type of fullerenes. Most importantly, the type-II, staggered, band alignment is formed between WS_2 (MoS_2) and fullerene with the latter possessing the higher electron affinity, resulting into the robust separation of photoexcited charge carriers between them. These results indicate that the electronic properties and photoactivity of TMDCs monolayers can be tuned by non-covalently coupled with small fullerenes, thus meeting the needs of various applications.

Keywords: 2D material; Fullerene; Heterostructures; Photoactivity; First-principles calculations

*. Corresponding author. *E-mail addresses:* wqhuang@hnu.edu.cn

#. Corresponding author. *E-mail address:* gfhuang@hnu.edu.cn

1. Introduction

Some significant developments have always been spearheaded by research into two-dimensional (2D) layered nanomaterials because of their potential applications in electronics, catalysis, biosensors, and energy storage [1, 2]. Among all of the studied 2D materials, TMDs, such as MoS_2 and WS_2, have received considerable attention owing to their extraordinary fundamental physical properties and application potentials in electronic devices [3]. TMDs have a formula of TX_2 and can occur in more than 40 different types depending on the combination of a transition metal (T ¼ Mo, W, Cr, V, etc.) and a chalcogen (X ¼ S, Se, Te, etc.). The electronic structures of TMDs vary from metallic (e.g. NbS_2 and VS_2) to semiconducting (e.g. MoS_2 and WS_2) [4, 5]. The versatility of electronic structures of TMDs offers opportunities for fundamental and technological research in a variety of fields [6].

In recent years, the use of carbonaceous materials such as fullerene, carbon nanotubes (CNTs) and graphene (GR) for the enhancement of photocatalytic performances of semiconductors has been demonstrated because of their special structures and unique electronic properties [7]. For instance, the fullerene/C_3N_4 heterostructures with efficient photocatalytic activity under visible light irradiation[8], and the GR/C_3N_4 heterostructures show high vis-light photocatalytic activity for hydrogen production [9]. GR, CNTs and fullerene have also been used to interface with TiO_2 to achieve extended photocatalytic activities well beyond that of pure TiO_2 materials. The enhanced photocatalytic performance of semiconductor/carbon heterostructures is generally attributed to the electron-accepting and transport properties of carbon nanomaterials since they provide a convenient way to direct the flow of photogenerated charge carriers [10].

Density functional theory (DFT) has been used to reveal the underlying mechanisms for superior photocatalytic performance of semiconductor/carbon nanomaterials. It has been demonstrated that coupling carbon nanomaterials can reduce the band gap of semiconductors, thus enhancing optical absorption in the visible region [11]. It is found that GR is the sensitizer for TiO_2 and g-C_3N_4, whereas significant charges transfer from anatase TiO_2 to GR is also reveal due to the different crystal structure [12]. First-principles DFT calculations exposed that GR/fullerenes (C_{60}, C_{70}, C_{80} and B_{80}) heterostructures is promote experimentalists to explore these systems, for their possible applications in electronic and opto-electronic devices [13]. It is reported that

fullerene/Ag_3PO_4 (MoS_2) heterostructures can effectively improve the photocatalytic active [14, 15]. The DFT calculations also suggested that C_{60}-interfaced TiO_2 in both the mechanical mixture and covalent linking cannot form an efficient photovoltaic heterostructures [16]. In addition, B- or N-doped C_{60} and MoS_2 or WS_2 monolayers can form an efficient photovoltaic heterostructures[17].

MoS_2 and WS_2 are also promising as tunable band gap semiconductor photocatalysts that may be more active than an archetypal photocatalytic material TiO_2 [18]. Bulk MoS_2 and WS_2 are indirect narrow band semiconductors, with band gap of 1.20 and 1.35 eV, which are inactive photocatalyst. Whereas their monolayer has direct band gap of 1.89 and 2.0 eV [3, 5], respectively. Moreover, the band gap, electron affinity, and ionization potential can be well engineered by applying mechanical strain or forming $Mo_{1-x}W_xS_2$ alloy [19].

More recently, several experimental studies showed that MoS_2 can be chemically functionalized with fullerenes, which possess an electron-accepting tendency [20, 21]. Consequently, it may be possible to tune the carrier types and concentrations of MoS_2 by adsorbing various fullerenes on the surface. Moreover, MoS_2/carbon-nanomaterials heterostructures have been attracting increasing attention due to their highly efficient vis-light photocatalytic performance. For instance, the MoS_2/GR heterostructures show superior vis-light-driven photocatalytic activity [22]. Similarly, it has been reported that TiO_2 grown on layered MoS_2/GR heterostructures show an enhanced photocatalytic H_2 evolution activity [23]. Similarly, MoS_2/CNT heterostructures exhibit high catalytic activity for electrocatalytic hydrogen evolution [24]. Compared with GR and CNTs, fullerene have been attracted particular interest owing to their functional characteristics and potential applications in the fields of nanomaterials and biomedical science. Therefore, it is expected to improve the photocatalytic performance of MoS_2 by fullerene modification, just as the case of C_{60}/TiO_2 [16]. Because WS_2 possesses semiconducting features similar to those of MoS_2, it is feasible to establish both monolayer MoS_2/fullerene and WS_2/fullerene heterostructures.

In this work, the structural and electronic properties of monolayer $WS_2(MoS_2)$/fullerene heterostructures have been investigated using large-scale DFT computations to explore the effects of non-covalent interactions on enhancing the photoactivity of monolayer $WS_2(MoS_2)$ by fullerene modification. Here, B_{12} and C_{20} are taken as the representative small fullerenes, motivated by

their special structure and properties. The fullerene B_{12} is predominantly constructed by the 3D icosahedral networks with electron deficient *mc*-2*e* bonds. Such crystal packing with B_{12} unit is found to be stable [13]. Whereas C_{20} consisting solely of pentagons, is the smallest unconventional fullerene which breaks the ‘‘isolated pentagon rule”. Moreover, these fullerenes are well established as single oxygen sensitizers for electron donor-acceptor assemblies and applies in the field of photocatalysis [25]. Most importantly, the MoS_2/C_{60} crystals has successfully prepared , and found that the inherent close proximity of photovoltaic-active MoS_2 monolayers to C_{60} molecules with strong electron affinities suggests a new kind of material for solar-cell applications with high quantum yields of photoinduced charge generation [20]. The role of fullerene in these photocatalytic systems can be speculated to be as follows: (1) it can form the space potential difference promoting the photogenerated electron-hole separation effectively; (2) it can tune the band gap by changing the band structure of the photocatalysts. The calculated results show that the band gap can be largely reduced due to interfacing with fullerene, resulting into a strong absorption in the entire visible region and thus superior photocatalytic activity. The electrostatic potential distribution in the interface, where the potential at WS_2 (MoS_2) is higher than that in fullerene, can effectively inhibit the electron-hole pair’s recombination and therefore improving its photocatalytic. This work would provide some new insight into optimizing the photocatalytic properties of WS_2 (MoS_2)-based or fullerene-based nanomaterial heterostructures.

2. Computational Method

In this work, we have performed a comprehensive first principles calculations to study the detailed properties of this heterogeneous structure to give the theoretical basis of the promoted photocatalytic activity [26, 27]. All calculations are performed using DFT, as implemented in the plane wave basis CASTEP code. The valence electrons considered were: W ($5s^25p^65d^46s^2$), Mo ($4s^24p^64d^55s^1$) and S ($3s^23p^4$), respectively. The local density approximation (LDA) with inclusion of the vdW interaction is chosen because long-range vdW interactions are expected to be significant in such these complexes. The cutoff energy for plane waves is chosen to be 400 eV. A Monkhorst-Pack mesh of k points, 2 × 2 × 1 and 4 × 4 × 1 points, is used, respectively, to sample the two-dimensional Brillouin zone for geometry optimization and for calculating the density of states, and the convergence tolerance of force on each atom during structure relaxation is set at

0.01 eV/Å [14].

For the monolayer WS_2 (MoS_2), the calculated lattice constant is in good agreement with the previous theoretical results. The monolayer WS_2 (MoS_2)/fullerene heterostructures are composited by using a supercell as illustrated in Fig. 1. The supercell (18.69 ×18.69 × 25.00 Å^3) contains B_{12}, C_{20} (containing 12 B and 20 C atoms, respectively) and one 6×6 monolayer WS_2 (MoS_2) (containing 36 W (Mo) and 72 S atoms). A vacuum layer of 15 Å is used in the direction normal to the interface, representing the isolated slab boundary condition. Note that there is no tensile or compressed deformation of WS_2 (MoS_2) surface in the *x*-*y* plane, different from other models (MoS_2/fullerene [15], Ag_3PO_4 (100)/fullerene [14], MoS_2/GR [28], TiO_2/CNT [29]).

The strong light absorption is one of fundamental premises for a high-efficiency photocatalyst. To explore the optical properties of pure WS_2, MoS_2, and WS_2 (MoS_2)/fullerene (B_{12} and C_{20}) heterostructures, their frequency-dependent dielectric matrixes are calculated by the Fermi golden rule within the dipole approximation. The imaginary part ε_2 ($\hbar\omega$) of the dielectric function due to direct interband transitions is given by the expression

$$\varepsilon_2(\hbar\omega) = \frac{2e^2\pi}{\Omega\varepsilon_0}\sum_{k,v,c}|\langle\Psi_k^c|u\cdot r|\Psi_k^v\rangle|^2\,\delta(E_k^c - E_k^v - E) \quad (1)$$

where *Ω, ω, u, v,* and *c* are the unit-cell volume, photon frequency, the vector defining the polarization of the incident electric field, valence bands, and conduction bands, respectively. The real part ε_1 of the dielectric function is obtained from ε_2 by a Kramers - Kronig transformation. Then, the optical absorption spectra are simulated by converting the complex dielectric function to the absorption coefficient αabs according to the following relation

$$I(\omega) = \sqrt{2}\omega\left[\sqrt{\varepsilon_1^2(\omega) + \varepsilon_2^2(\omega)} - \varepsilon_1(\omega)\right]^{1/2} \quad (2)$$

Taking into account the tensor nature of the dielectric function, $\varepsilon_1(\omega)$ and $\varepsilon_2(\omega)$ are averaged over three polarization vectors (along x, y, and z directions). All other optical constants can also be obtained. The relations above are the theoretical basis of band structure and optical properties analyzing which reflected the mechanism of absorption spectral caused by electronic transition between different energy levels.

3. Results and Discussion

3.1. Geometric Structure and Electronic Properties

Fig. 1 present the fully optimized geometric structures of the monolayer WS_2 (MoS_2)/fullerene heterostructures. Parts a and c respectively present the top and side views between monolayer WS_2 and B_{12} heterostructures, whereas parts b and d displays the side views of the MoS_2/B_{12} and WS_2/C_{20} heterostructures used in our calculations. Geometry optimizations have first been performed for all of the systems using the conjugate gradient method. The equilibrium distances between fullerene and the top-most atoms of the monolayer WS_2 (MoS_2) are around 2.76, 2.81 and 2.71 Å for MoS_2/B_{12}, WS_2/B_{12} and WS_2/C_{20} (as listed in Table 1), respectively, which is about equal to those between the GR sheet and other materials (2.85 Å for TiO_2(001)/GR [30], 3.32 Å MoS_2/GR [31]). The smaller distance shows that the interaction between monolayer WS_2 and C_{20} is stronger than that between monolayer WS_2 (MoS_2) and B_{12}. After optimization, the WS_2 (MoS_2) and fullerene are nearly unchanged, which is a typical vdW equilibrium spacing, rather than covalent, in accordance with the others' results [17]. To address the thermodynamic stability of the WS_2 (MoS_2)/fullerene heterostructures, one can calculate the interface adhesion formation energy, which is defined as:

$$E_{ad} = E_{comb} - E_{fullerene} - E_{WS_2(MoS_2)} \quad (3)$$

where E_{comb}, $E_{fullerene}$, and $E_{WS_2(MoS_2)}$ represent the total energy of the relaxed WS_2 (MoS_2)/fullerene, pure fullerene, and pure WS_2 (MoS_2), respectively. By this definition, negative E_{ad} suggests that the adsorption is stable. The interface formation energy is calculated to be -1.41, -0.88, -1.37 eV for the MoS_2/B_{12}, WS_2/B_{12} and WS_2/C_{20} heterostructures, respectively, which indicates a rather strong interaction between monolayer WS_2 (MoS_2) and fullerene heterostructures, and the high thermodynamically stability of these heterostructures. Compared with this results, the MoS_2/B_{12} heterostructures with lower adhesion energy can form more easily.

3.2. Density of States

To explore the influence of vdW interaction on the electronic properties of WS_2 (MoS_2), we have calculated the total density of states (TDOSs) and the project density of state (PDOS) of individual WS_2 (MoS_2), fullerene, and their heterostructures, as shown in Fig. 2. Pure monolayer WS_2 (MoS_2) is a direct semiconductor with a band gap (E_g) of 2.03 (1.89) eV, which is comparable to the MoS_2 photoluminescence experiment and previous theoretical studies (~2.1 (1.9) eV) [26, 32]. The bottom of conduction band (CB) of pure MoS_2 (WS_2) is mainly constituted of Mo 4d and S 3d

(W 5d) states, whereas the upper part of valence band (VB) is composed of Mo 4d (W 5d and S 3p) states. This is one of the most important factors for the lower photocatalytic properties of pure WS_2 (MoS_2). The calculated DOSs show that band gap for individual B_{12} is 2.01 eV, which is comparable to the theoretical value of 1.3-2.0 eV [33]. While the band gap for individual C_{20} is 1.90 eV, in agreement well with the value of 1.94 eV with using hybrid B3LYP functional calculations [34], and 1.95 eV with B3LYP/6-31G density functional level of theory calculations [35]. Therefore, the LDA method is also effective method to correctly characterize the electronic structures of the specific WS_2 monolayer and C_{20} fullerene.

The calculated DOSs of the above three heterostructures characterize the interface electronic properties and energy levels alignment in detail, as shown in Fig. 2. The calculated band gaps of three heterostructures are 1.31, 1.45, and 0.93 eV, respectively, as listed in Table 1. The reduced band gaps can make the heterostructures absorb the most sunlight, and the photogenerated electron transfer from the VBM to the CBM of the monolayer WS_2 (MoS_2)/fullerene heterostructures becomes easier. Interestingly, for the WS_2/C_{20} (B_{12}) heterostructures, the VBM is mainly occupy by S 3p and W 5d orbital, whereas the CBM is compose of C 2p (B 2s and 2p) orbitals. In the MoS_2/B_{12} heterostructures, the VBM is mainly occupied by S 3p and Mo 4d orbital, the CBM is composed of B 2s and 2p orbitals. The VBM of WS_2 (MoS_2) is higher than that of C_{20} (B_{12}), whereas the CBM of C_{20} (B_{12}) is lower than that of WS_2 (MoS_2). On the basis of the above analysis, we find that the WS_2 (MoS_2)/fullerene heterostructures is a typical type-II band alignment structure, which can be more clearly seen from the electron density distributions of the highest occupied and lowest unoccupied levels (HOL and LUL), respectively, as shown in Fig. 3. Fig. 3 (a1-c1) clearly displays that the HOL is only composed of the C 2p, B 2p and 2s orbits, respectively, while (a2-c2) is composed of the W 5d, Mo 4d, mixing with small S 3p orbits. In photocatalysis, such band alignment is beneficial for the separation of electron-hole pairs. Thus, the fullerene would be a sensitizer for WS_2 (MoS_2). These results indicate that choosing appropriate fullerene (such as B_{12} and C_{20}) is especially critical to obtain high efficiency of electron-hole separation in the monolayer WS_2 (MoS_2)/fullerene heterostructures.

3.2. Charge Density Difference and Mechanism Analysis

To explore the charge transfer and separation at the WS_2 (MoS_2)/fullerene heterostructures,

the charge density difference of WS_2 (MoS_2)/fullerene heterostructures is calculated, and the results are depicted in Fig. 4b, c and e. The green region represents charge depletion, and the purple region indicates charge accumulation. Due to the interaction, a very interesting charge redistribution at the monolayer WS_2 (MoS_2)/fullerene heterostructures can be obviously observed. A strong charge accumulation mainly from the bottom-most B(C) atoms of the fullerene and some from the charge loosed by S atoms along the Z axis just under the B(C) atom rings, is found just above the top-most S atoms. Moreover, the charge redistribution at the bottom-most B atoms and the top-most S atoms becomes more significant as the 2D material is different (comparing Fig. 4c with e), which is consistent with the shorter interface distance and stronger interaction. In the Fig. 4b and e, the charge redistribution at the bottom-most B(C) atoms and the top-most S atoms becomes more significant as the fullerene is different. Note that the electron losses of different C atoms in the bottom-most and of different S atoms vary with their positions, owing to the different atomic arrangement. Most importantly, closer inspection to Fig. 4b, c and e reveals that the slightly interaction results into the negatively charged W (Mo) atoms in the monolayer WS_2 (MoS_2). This indicates that some W (Mo) atoms at basal planes, initially catalytically inert, would turn out to be active sites, which are beneficial to the improved photocatalytic performance of the monolayer WS_2 (MoS_2)/fullerene heterostructures.

The planar-averaged charge density difference along the Z direction exhibited change of charge density, which is illustrated in Fig. 4d. The positive values represent electron accumulation, and the negative values indicate electron depletion. The change at interfaces indicates that the electrons transfer from the fullerene to the WS_2 (MoS_2) across the interface, whereas the holes remain in the fullerene side. It is clear that the largest efficient electron accumulation localized above the top-most S atoms is about 3.0×10^{-4} e/Å^3, the largest local efficient electron depletion at the bottom-most B atoms is about -1.19×10^{-4} e/Å^3 in the MoS_2/B_{12} heterostructures, while in the $WS_2/B_{12}(C_{20})$ heterostructures, the largest efficient electron accumulation localized above the top-most S atoms is about 1.85×10^{-4} e/Å^3 (0.78×10^{-4} e/Å^3), and the largest local efficient electron depletion localized above the W atoms is about -1.02×10^{-4} e/Å^3 (-0.68×10^{-4} e/Å^3). This indicates that the charge transfer is related to the interface distance or vdW interaction.

To quantify analyze the charge variation at the interface, the Mulliken population analysis of

the plane-wave pseudopotential calculations has been performed on the fullerene, isolated monolayer WS_2 (MoS_2), and WS_2 (MoS_2)/fullerene heterostructures. Fig. 5 shows the results of the Mulliken charge on different atoms, in which several typical values are presented. For the isolated monolayer WS_2 (MoS_2), the S and W (Mo) atoms have a Mulliken charge of 0.01 and -0.02, respectively. The interfacial interaction leads to a markedly change of Mulliken charge of each atom in the WS_2 (MoS_2) of the heterostructures, while the W (Mo) atoms become -0.03, -0.02 (-0.02, -0.01) in the WS_2/B_{12} (C_{20}) (MoS_2/B_{12}) heterostructures, respectively, indicating that the electron of W (Mo) atoms of monolayer WS_2 (MoS_2) is changed due to the coupling of fullerene. The top-most S atoms of monolayer WS_2 (MoS_2) have a Mulliken charge of 0.02, 0.03 (MoS_2/B_{12}), 0.03 (WS_2/B_{12}), 0.04, 0.03, 0.02 (WS_2/C_{20}) respectively. The charge variation demonstrates that the top-most S atoms of the WS_2 (MoS_2)/fullerene heterostructures would lose more electrons than those in isolated monolayer WS_2 (MoS_2). This would improve the stability of monolayer WS_2 (MoS_2)/fullerene photocatalyst, just as the case of MoS_2/GR [36]. Although the B and C atom in the fullerene has a Mulliken charge of approach zero electrons, those B(C) atoms in the WS_2 (MoS_2)/fullerene heterostructures have different Mulliken charges because not only the arrangement of atoms under various B(C) atoms is different, but also the interface interaction is varied. For example, Fig. 5b shows that, in the WS_2/C_{20} heterostructures, the C atom has a Mulliken charge of -0.05, -0.03, -0.01. Those B atoms in the WS_2/B_{12} heterostructures have a Mulliken charge of -0.05 and -0.06, whereas in the MoS_2/B_{12} heterostructures, B atoms have a Mulliken charge of -0.07 and -0.04. As a result, the charge distribution fluctuations appear at the bottom-most B(C) atoms due to the interactions between monolayer WS_2(MoS_2) and fullerene. The effective net charge from one constituent to another in these composites can be analyzed on the basis of the Bader method, as listed in Table 1. Some electrons transfer from fullerene to WS_2 (MoS_2) in the WS_2 (MoS_2)/fullerene heterostructures. The result indicates that 0.18 electrons transfer from B_{12} to the MoS_2 at the MoS_2/B_{12} heterostructures. Whereas 0.12 (0.03) electrons transfer from B_{12} (C_{20}) to the WS_2 at the WS_2/B_{12} (C_{20}) heterostructures. Net charge accumulation is helpful to the separation of electrons and holes. To understand the origin of such an interface electron transfer in these heterostructures, work functions for the fullerene and monolayer WS_2 (MoS_2) are calculated by aligning the Fermi level relative to the vacuum energy level. They are

calculated to be 4.45, 4.45, 5.37 and 5.35 eV for B_{12}, C_{20}, monolayer WS_2 and MoS_2, respectively. The spontaneous interfacial charge transfer in these heterostructures can be simply rationalized in terms of the difference on their work functions.

The interface charge redistribution would surely alter the electrostatic potential distribution in whole system. To conduct quantitative analysis, the profile of the planar averaged self-consistent electrostatic potential for the monolayer WS_2 (MoS_2)/fullerene heterostructures as a function of position in the z-direction is displayed in Fig. 4a. Surprisingly, the electrostatic potential at the middle region of the interface is close to zero, due to charge redistribution. It is well known that the monolayer WS_2 (MoS_2) is a typical S-W (Mo)-S sandwich structure. The potential at the W (Mo) atomic plane is higher than that at the fullerene, resulting into a large potential difference between the two constituents. The built-in potential would be one of the important factors for improving the photocatalytic activity and stability of monolayer WS_2 (MoS_2)/fullerene photocatalyst. Under light irradiation, the separation and migration of photogenerated carriers at the interface will be affected by this built-in potential, i.e., the existence of a potential well can effectively hinder the recombination of photogenerated charge carriers in the monolayer WS_2 (MoS_2)/fullerene heterostructures. Therefore, the photocatalytic activity and stability of WS_2 (MoS_2) photocatalyst can be improved by coupling fullerene.

3.3. Optical Properties

For many semiconductors (for example, TiO_2 [37], CeO_2 [38], SnO_2 [39], $SrTiO_3$ [40], Ag_3PO_4 [41], and g-C_3N_4 [12]) with wide band gap, the incorporated GR sheet can extend their absorption edge to the visible light region and enhance their photocatalytic activity. Similarly, coupling fullerene with semiconductors is also an effective strategy to extend the absorption edge and enhance the photocatalytic activity. To explore the influence of the coupled fullerene on the light absorption of WS_2 (MoS_2), the imaginary part of the dielectric function and visible absorption spectra of monolayer WS_2 (MoS_2) and the monolayer WS_2 (MoS_2)/fullerene heterostructures are calculated, as shown in Fig. 6. For the monolayer WS_2 (MoS_2), the optical absorption occurs at about 2.03 (1.89) eV [26], which is attributed to the intrinsic transition from the W(Mo) 5d(4d) to S 3p orbitals. As can be clearly seen from Fig. 6, the absorption intensity of WS_2 (MoS_2)/fullerene heterostructures is enhanced in the visible light region compared to the monolayer WS_2 (MoS_2).

Note that compared to that of the monolayer MoS_2/fullerene heterostructure, the enhancement of optical absorption of WS_2/fullerene is more obvious and more range of wavelength in visible light region. Miraculously the shape of absorption curve of the monolayer WS_2 (MoS_2)/fullerene heterostructures depends on the fullerene types (see Fig. 6(b)), indicating that the electronic transitions are different. In the region from 300 to 380 nm and 600 to 700 nm, the absorption of WS_2/B_{12} heterostructures is higher than that of MoS_2/B_{12} heterostructures, but in the region from 380 to 600 nm, the absorption of MoS_2/B_{12} heterostructures is higher than that of the WS_2/B_{12} heterostructures. Simultaneously, in the region from 300 to 560 nm, the absorption of WS_2/C_{20} heterostructures is higher than that of WS_2/B_{12} heterostructures, whereas in the region from 560 to 700 nm, the absorption of WS_2/B_{12} heterostructures is higher than that of WS_2/C_{20} heterostructures. These distinctions can be attributed to the difference of electronic structures, especially those near the band gap (Fig. 2 and 3). Thus, it is reasonable to conclude that coupling fullerene on the WS_2 would lead to the enhanced absorption in the visible region, which would be one of the most important factors to improve the photoactivity of monolayer WS_2.

4. Summary

In summary, the electronic structures of the WS_2 (MoS_2)/fullerene, monolayer WS_2 (MoS_2), and fullerene have been investigated by using first-principles calculations based on DFT. We have studied changes in the electronic structure, charge transfer and photoactivity of WS_2 (MoS_2) in the presence of small fullerenes. It is unveiled that the fullerene can act as a sensitizer in monolayer WS_2 (MoS_2) to improve the photoactivity. Compared to pure monolayers, the heterostructures have smaller band gap (1.31, 1.45 and 0.93 eV), which is in favor of enhancing the visible light absorption. The type-II, staggered, band alignment is formed between WS_2 (MoS_2) and fullerene with the latter possessing the higher electron affinity, resulting into the robust separation of photoexcited charge carriers between them. It is expected that B_{12} and C_{20} acts as a sensitizer in other fullerene-semiconductor heterostructures. This strongly suggests possible applications in photocatalysis. Our results provide novel insight into the understanding of the effect of heterostructures, which will help not only in understanding the mechanism of photocatalysis but also in designing new heterostructures for photocatalytic reactions.

Acknowledgements

This work was supported by the National Natural Science Foundation of China (Grant Nos. 51471068 and 51428101).

References

1. R. Asahi, T. Morikawa, T. Ohwaki, K. Aoki and Y. Taga, *Science*, 2001, **293**, 269-271.
2. Z. G. Zou, J. H. Ye, K. Sayama and H. Arakawa, *Nature*, 2001, **414**, 625-627.
3. H. Shi, H. Pan, Y. W. Zhang and B. I. Yakobson, *Physical Review B: Condensed Matter and Materials Physics*, 2013, **87**, 155304.
4. W. Zhou, Z. Yin, Y. Du, X. Huang, Z. Zeng, Z. Fan, H. Liu, J. Wang and H. Zhang, *Small*, 2013, **9**, 140-147.
5. K. Kośmider and J. Fernández-Rossier, *Physical Review B: Condensed Matter and Materials Physics*, 2013, **87**, 075451.
6. B. Amin, N. Singh and U. Schwingenschloegl, *Physical Review B: Condensed Matter and Materials Physics*, 2015, **92**, 075439.
7. Y. H. Zhang, Z. R. Tang, X. Z. Fu and Y. J. Xu, *ACS Nano*, 2011, **5**, 7426-7435.
8. Q. J. Xiang, J. G. Yu and M. Jaroniec, *Journal of Physical Chemistry C*, 2011, **115**, 7355-7363.
9. Y. Zhang, T. Mori, L. Niu and J. Ye, *Energy & Environmental Science*, 2011, **4**, 4517-4521.
10. H. Chen, Y. Xie, X. Sun, M. Lv, F. Wu, L. Zhang, L. Li and X. Xu, *Dalton Transactions*, 2015, **44**, 13030-13039.
11. N. Umezawa, O. Shuxin and J. Ye, *Physical Review B*, 2011, **83**, 035202.
12. J. G. Yu, S. H. Wang, J. X. Low and W. Xiao, *Physical Chemistry Chemical Physics*, 2013, **15**, 16883-16890.
13. A. K. Manna and S. K. Pati, *Chemphyschem*, 2013, **14**, 1844-1852.
14. C. Y. Luo, W. Q. Huang, L. Xu, Y. C. Yang, X. Li, W. Hu, P. Peng and G. F. Huang, *Physical chemistry chemical physics*, 2016, **18**, 2878-2886.
15. C.Y. Luo, W.Q. Huang, L. Xu, Y.C. Yang, X. Li, W. Hu, P. Peng and G.F. Huang, *RSC Advances*, 2016, **6**, 43228-43236.
16. R. Long, Y. Dai and B. Huang, *Journal of Physical Chemistry Letters,* 2013, **4**, 2223−2229.
17. L. Y. Gan, Q. Zhang, Y. Cheng and U. Schwingenschlogl, *Journal of Physical Chemistry*

Letters, 2014, **5**, 1445-1449.

18. G. Hua, S. Yin, Y. Xia, S. Zhigang and L. Banggui, *Journal of Physics: Condensed Matter*, 2006, **18**, 87-96.
19. J. Kang, S. Tongay, J. Zhou, J. Li and J. Wu, *Applied Physics Letters*, 2013, **102**, 012111.
20. M. Remskar, A. Mrzel, A. Jesih, J. Kovac, H. Cohen, R. Sanjines and F. Levy, *Advanced Materials*, 2005, **17**, 911-914.
21. Y. Tan, K. Yu, T. Yang, Q. Zhang, W. Cong, H. Yin, Z. Zhang, Y. Chen and Z. Zhu, *Journal of Materials Chemistry C*, 2014, **2**, 5422.
22. Q. Li, N. Zhang, Y. Yang, G. Wang and D. H. Ng, *Langmuir : the ACS journal of surfaces and colloids*, 2014, **30**, 8965-8972.
23. Y. Yuan, X. Gong and H. Wang, *Physical Chemistry Chemical Physics*, 2015, **17**, 11375-11381.
24. V. O. Koroteev, L. G. Bulusheva, I. P. Asanov, E. V. Shlyakhova, D. V. Vyalikh and A. V. Okotrub, *Journal of Physical Chemistry C*, 2011, **115**, 21199-21204.
25. K. H. Lee, J. Y. Lee and Y. G. Hwang, *Bulletin of the Korean Chemical Society*, 2013, **34**, 365-366.
26. A. Ramirez-Torres, D. Le and T. S. Rahman, *IOP Conference Series: Materials Science and Engineering,* 2015, **76**, 012011.
27. Y. Li, Y.L. Li, C. M. Araujo, W. Luo and R. Ahuja, *Catalysis Science & Technology*, 2013, **3**, 2214.
28. X. An and J. C. Yu, *RSC Advances*, 2011, **1**, 1426-1434.
29. K. Woan, G. Pyrgiotakis and W. Sigmund, *Advanced Materials*, 2009, **21**, 2233-2239.
30. P. Zhou, X. F. Zhu, J. G. Yu and W. Xiao, *ACS Appl. Mater. Interfaces*, 2013, **5**, 8165-8172.
31. Y. Ma, Y. Dai, M. Guo, C. Niu and B. Huang, *Nanoscale*, 2011, **3**, 3883-3887.
32. A. Kuc, N. Zibouche and T. Heine, *Physical Review B: Condensed Matter*, 2011, **83**, 245213.
33. R. Franz and H. Werheit, *EPL (Europhysics Letters)*, 1989, **9**, 145.
34. Y. Cao, D. W. Wang, B. Liu, G. J. Yao, Y. T. Fu, X. J. Li and Z. G. Bi, *International Journal of Quantum Chemistry*, 2013, **113**, 1440-1446.
35. Z. Chen, H. Jiao, M. Bühl, A. Hirsch and W. Thiel, *Theoretical Chemistry Accounts*, 2001, **106**, 352-363.

36. W. Y. Zan, W. Geng, H. X. Liu and X. J. Yao, *Journal of Alloys and Compounds*, 2015, **649**, 961-967.

37. R. Long, Y. Dai and B. Huang, *The Journal of Physical Chemistry Letters*, 2013, **4**, 2223-2229.

38. Z. M. Yang, G. F. Huang, W. Q. Huang, J. M. Wei, X. G. Yan, Y. Y. Liu, C. Jiao, Z. Wan and A. Pan, *Journal of Materials Chemistry A,* 2014, **2**, 1750-1756.

39. S. S. Ding, W. Q. Huang, Y. C. Yang, B. X. Zhou, W. Y. Hu, M. Q. Long, P. Peng and G. F. Huang, *Journal of Applied Physics*, 2016, **119**, 205704.

40. S. Kumar, S. Tonda, A. Baruah, B. Kumar and V. Shanker, *Dalton Transactions*, 2014, **43**, 16105-16114.

41. C. N. He, W. Q. Huang, L. Xu, Y. C. Yang, B. X. Zhou, G. F. Huang, P. Peng and W. M. Liu, *Scientific Reports,* 2016, **6**, 22267.

Structure	E_{ad}(eV)	E_g(eV)	d(Å)	Bader Charge (e)	
				$WS_2(MoS_2)$	B(C)
MoS_2/B_{12}	-1.41	1.31	2.76	-0.18	0.18
WS_2/B_{12}	-0.88	1.45	2.81	-0.12	0.12
WS_2/C_{20}	-1.37	0.93	2.71	-0.03	0.03

Table 1: The adhesion energy (E_{ad}), band gap (E_g), mean distance (d) of optimized MoS_2/B_{12}, WS_2/B_{12}, and WS_2/C_{20} heterostructures.

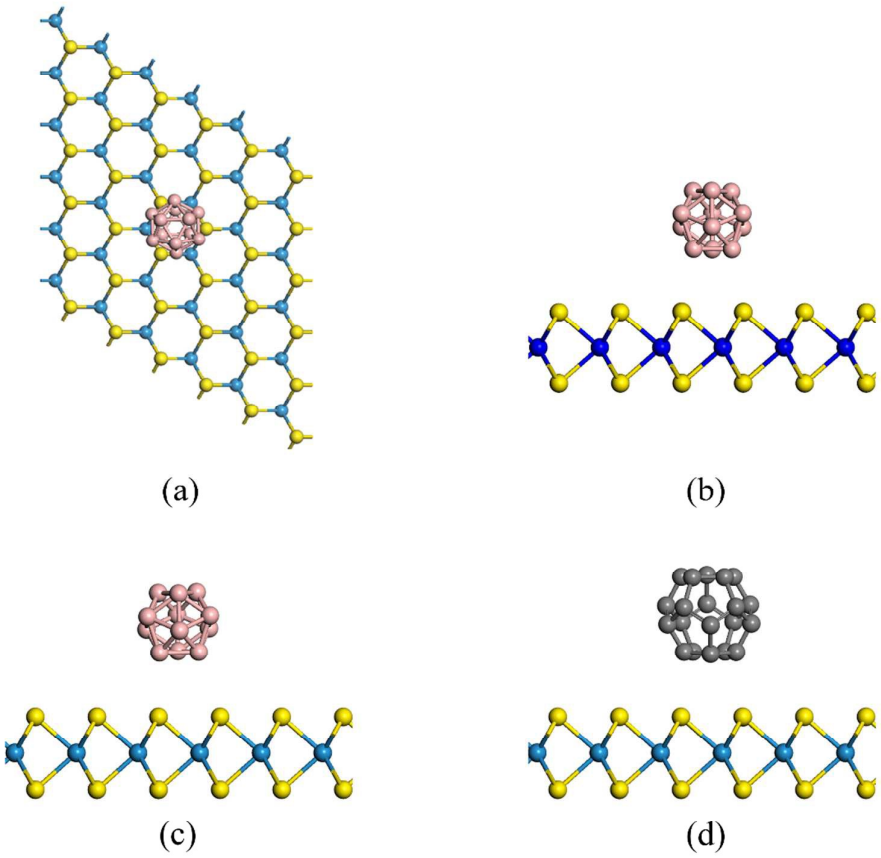

Figure 1: The (a) top , (c) and (d) side view of the simulating interface between B_{12} , C_{20} and WS_2 heterostructures, (b) side view of the simulating interface between B_{12} and MoS_2 heterostructures. Gray, pink, blue, green and yellow spheres represent C, B, Mo, W and S atoms, respectively.

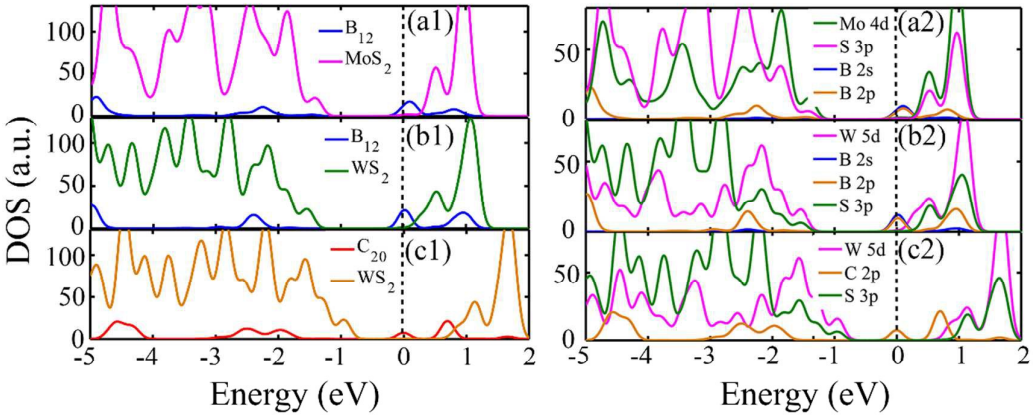

Figure 2: DOS for (a1-c1) MoS_2/B_{12}, WS_2/B_{12}, and WS_2/C_{20} heterostructures; (a2) PDOS of Mo, S and B atoms in MoS_2/B_{12} heterostructures; (b2) PDOS of W, S and B atoms in WS_2/B_{12} heterostructures; (c2) PDOS of W, S and C atoms in WS_2/C_{20} heterostructures; respectively. The Fermi level is set to zero energy.

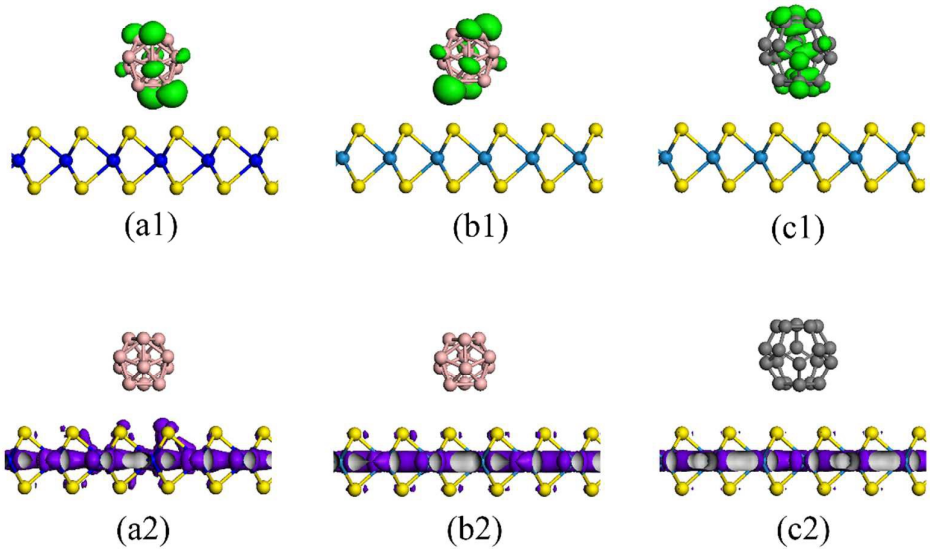

Figure 3: Maps of the charge density distributions of the lowest unoccupied (upper panel) and highest occupied levels (lower panel). (a-c) are for the MoS_2/B_{12}, WS_2/B_{12}, and WS_2/C_{20} heterostructures, respectively. The isovalue is 0.004 e/Å^3.

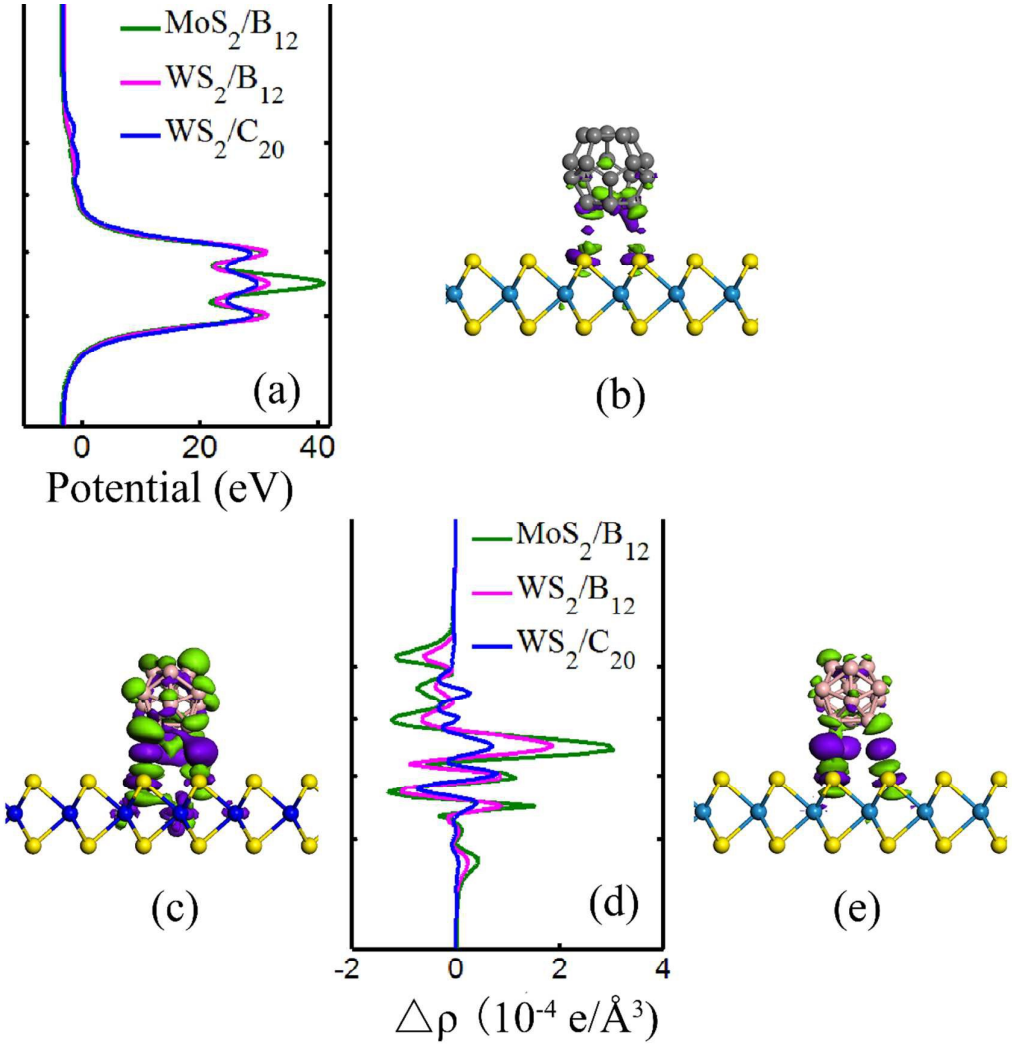

Figure 4: 3D Charge density differences for (b) MoS_2/B_{12}, (c) WS_2/B_{12}, and (e) WS_2/C_{20} heterostructures. The purple and green represent charge accumulation and depletion, respectively. The isovalue is 0.004 e/Å^3. (a) Profile of the planar averaged self-consistent electrostatic potential for the MoS_2/B_{12}, WS_2/B_{12} and WS_2/C_{20} as a function of position in the z-direction. (d) Profile of the planar averaged charge density difference for the MoS_2/B_{12}, WS_2/B_{12} and WS_2/C_{20} as a function of position in the z-direction, respectively.

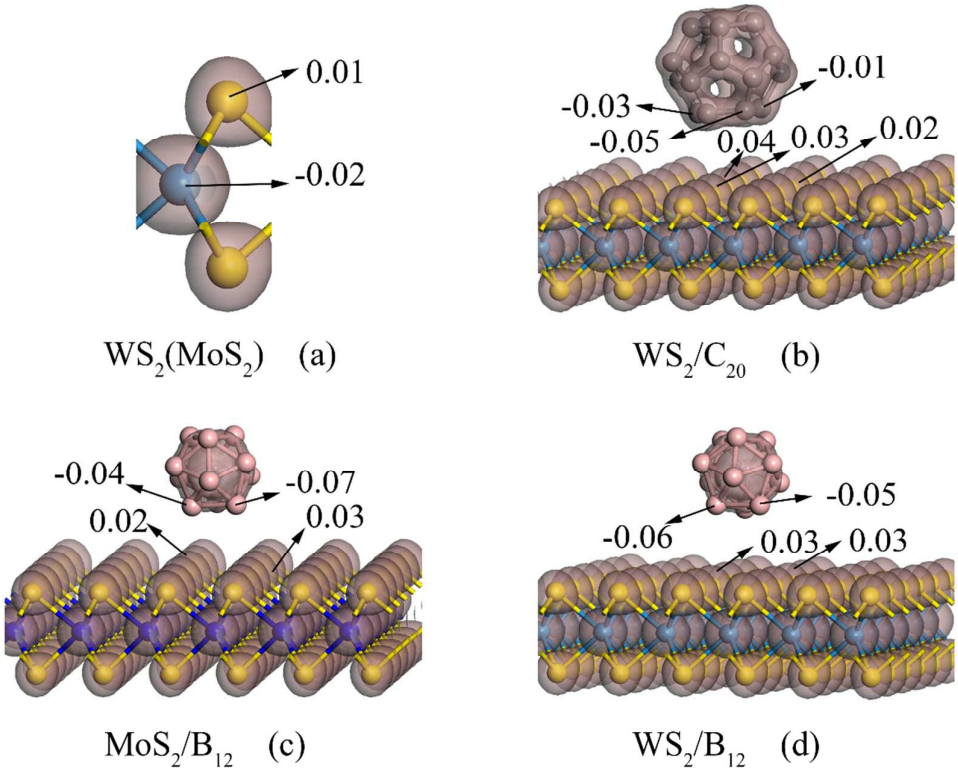

Figure 5. Charge distribution maps of (a) $WS_2(MoS_2)$, (b) WS_2/C_{20}, (c) MoS_2/B_{12}, and (d) WS_2/B_{12}, with an isovalue of 0.8 e/Å^3. Gray, pink, blue, green and yellow spheres represent C, B, Mo, W and S atoms, respectively.

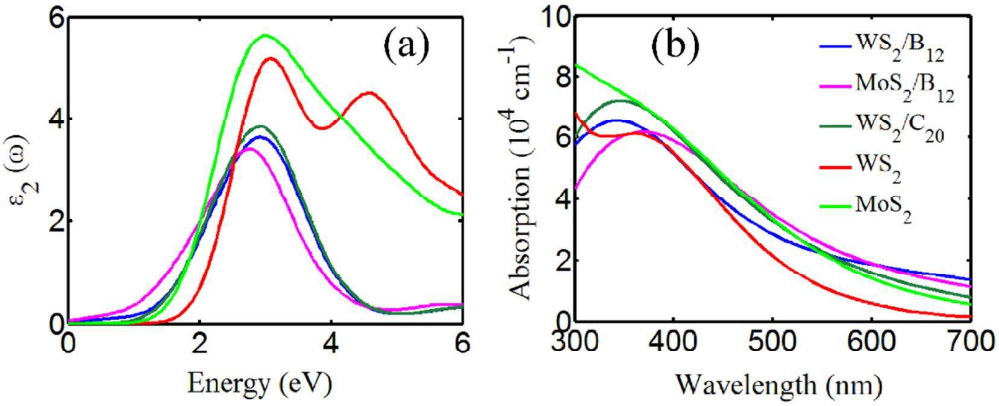

Figure 6: Calculated (a) imaginary part of the dielectric function and (b) absorption spectra of the WS_2/B_{12} (blue line), MoS_2/B_{12} (rose red line), WS_2/C_{20} (deep green line), WS_2 (red line) and MoS_2 (green line) heterostructures, respectively.

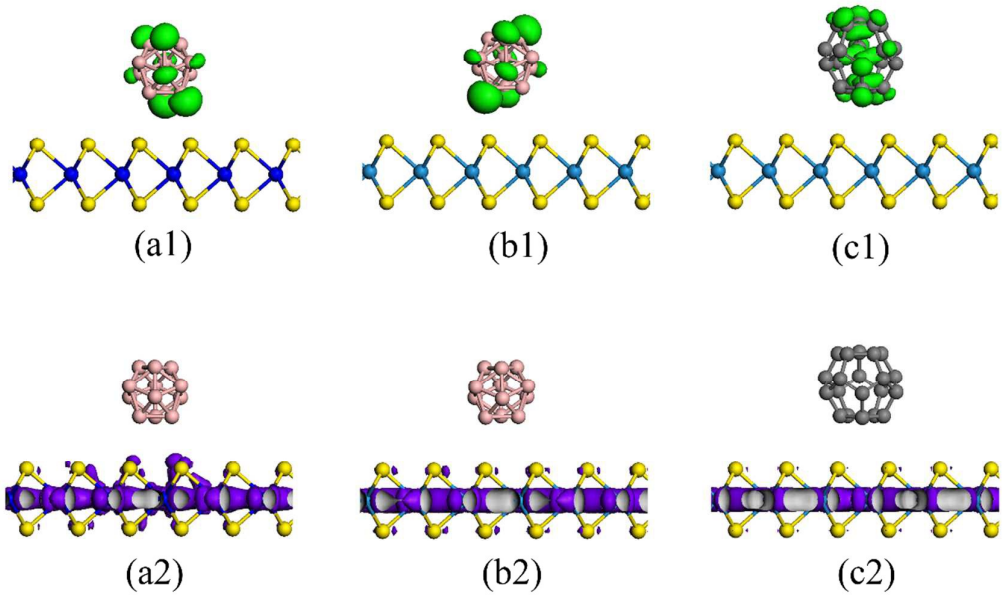

Graphical Abstract